International Symposium
On Turbulence and Shear Flow
Phenomena (TSFP-9)
June 30 - July 3, 2015 Melbourne, Australia

PIV STUDY OF A 3D TURBULENT OFFSET JET FLOW OVER SQUARE RIBS

Baafour Nyantekyi-Kwakye
Department of Mechanical Engineering
University of Manitoba
75A Chancellors Circle, Winnipeg, Manitoba, R3T 5V6, Canada
umnyankt@myumanitoba.ca

Mohammad Shajid Rahman
Department of Mechanical Engineering
University of Manitoba
75A Chancellors Circle, Winnipeg, Manitoba, R3T 5V6, Canada
rahmanms@myumanitoba.ca

Sarah Boila
Department of Civil Engineering
University of Manitoba
75A Chancellors Circle, Winnipeg, Manitoba, R3T 5V6, Canada
umboilas@myumanitoba.ca

Shawn P. Clark
Department of Civil Engineering
University of Manitoba
75A Chancellors Circle, Winnipeg, Manitoba, R3T 5V6, Canada
shawn.clark@umanitoba.ca

Mark F. Tachie
Department of Mechanical Engineering
University of Manitoba
75A Chancellors Circle, Winnipeg, Manitoba, R3T 5V6, Canada
mark.tachie@umanitoba.ca

ABSTRACT

An experimental study was conducted to investigate a three-dimensional offset jet flow over a surface mounted square rib using particle image velocimetry. The square rib was mounted at three different streamwise locations, $1.25b_o$, $3.45b_o$ and $6.25b_o$ from the nozzle exit (where b_o is the nozzle height). An increase in reattachment length of the offset jet was observed when the placement of the rib was increased from the nozzle exit. Increasing the location of the rib from the nozzle exit resulted in a faster decay of the maximum streamwise mean velocity. In the near-field of the jet, the rib location modified the turbulent kinetic energy, Reynolds shear stress and triple velocity correlations. Results from the Reynolds normal stresses highlighted the highly anisotropic nature of the flow field of three-dimensional offset jets. A quadrant analysis revealed that all four events were affected by changing rib location. Contrary to boundary layers both interaction events contributed to the total Reynolds shear stress.

INTRODUCTION

Three dimensional (3D) offset jets are encountered in diverse engineering and environmental applications such as fuel injection systems, environmental transport and mixing of effluent in lakes and rivers as well as in energy dissipation structures. The flow field of an offset jet can be divided into the following three main regions: recirculation, reattachment and wall jet region. The features of the recirculation and reattachment regions are qualitatively similar to prototypical separated and reattached turbulent shear flows. The wall jet flow, which is formed downstream of the reattachment region, is a composite shear layer with an inner region that is similar to a turbulent boundary layer, and an outer region that is akin to a free jet. In view of their complex flow physics, refined measurements in turbulent offset jets are essential to optimize a multitude of mixing devices, and also to provide the physical understanding and benchmark datasets required to facilitate the development of accurate numerical models and validate numerical results.

Considerable research efforts have been made in the past to advance our understanding of two-dimensional (2D) offset jets (Bhuiyan et al. 2011; Nasr and Lai, 1998; Pelfrey and Liburdy, 1986). On the other hand, only few investigations on the relatively more complex 3D offset jets have been reported (Nyantekyi-Kwakye et al. 2014; Agelinchaab and Tachie, 2011). As a consequence, our understanding of the flow physics for 3D offset jets is deficient compared with their 2D counterparts and other canonical turbulent shear flows. Agelinchaab and Tachie (2011) investigated the effects of Reynolds number and offset height on the reattachment length and turbulent transport phenomena in 3D offset jets. The experiments, which were performed using a particle image velocimetry (PIV), were conducted at three Reynolds numbers, Re = 5000, 10000 and 20000 and four offset height ratio, h/b_o = 0, 0.5, 1.5 and 3.5 (where h is the offset height and b_o is the nozzle height, $h/b_o = 0$ corresponds to generic wall jet). The results revealed that the reattachment length was independent of Reynolds number but increased with increasing offset height ratio. The development of the mean flow and higher order turbulence statistics showed a distinct dependence on h/b_o. For example, the mean velocity profiles required a longer x/b_o (where x is the streamwise distance with the origin at the nozzle exit) to

attain self-similarity when h/b_o was changed from 0.5 to 3.5.

Recently, an experimental research program was initiated to study the effects of offset height ratio on the characteristics of 3D offset jets produced from a sharp-edged rectangular slot in an open channel (Nyantekyi-Kwakye et al. 2014). The measurements were performed at a fixed Reynolds number of 8000 and 3 offset height ratios of h/b_o = 0, 2 and 4. The reattachment lengths (L_e) for h/b_o = 2 and 4 were, respectively, L_e/b_o = 4.4 and 6.2. As expected, the lateral spread rate was larger than the wall-normal spread rate, irrespective of h/b_o. However, both lateral and wall-normal spread rates decreased with increasing h/b_o.

The focus of the present study is to understand the flow characteristics and turbulent transport phenomena in 3D offset jets over a surface mounted 2D square rib. Specifically, initial conditions such as inlet Reynolds number, Froude number and offset height were kept constant while the streamwise location of the square rib on the wall was varied to investigate the impact on the recirculation and reattachment region as well as the wall jet region.

EXPERIMENTAL SETUP AND PROCEDURE

The experiments were performed in an open channel with dimensions 2500 mm long and a square cross section of 200 × 200 mm. The side walls as well as the bottom of the test section were made from a smooth acrylic to facilitate optical access. The Cartesian coordinate system was used with x and y representing the streamwise and wall-normal distances, respectively. The 3D offset jet was generated from a rectangular nozzle with dimensions 8 mm high (b_o) and 48 mm wide. The experiments were conducted for an offset height ratio (h/b_o) of 2. A 2D acrylic rib of 10 × 10 mm square cross section as shown in Fig. 1, spanning the entire channel width was positioned at x/b_o = 1.25, 3.45 and 6.25 from the nozzle exit which are represented herein as $R1$, $R2$ and $R3$, respectively. Locations $R1$, $R2$ and $R3$ corresponded to streamwise locations within the recirculation, reattachment and developing regions, respectively, of a reference experiments performed at similar test conditions but with no rib mounted on the wall (Nyantekyi-Kwakye et al. 2014). The tailwater depth, y_t, was maintained constant at 116 mm. The bulk velocity, U_o, of the flow was 0.95 ms^{-1} yielding a Reynolds number (Re = $(b_oU_o)/\nu$) and Froude number (Fr = $U_o/(gb_o)^{0.5}$) of 7600 and 3.4, respectively, where ν is the kinematic viscosity of water and g is the acceleration due to gravity.

The velocity measurements were performed using a planar particle image velocimetry system. The flow was seeded with 10 μm silver coated hollow glass spheres having a specific gravity of 1.4. A New Wave Solo Nd:YAG double-pulsed laser with maximum energy of 120 mJ per pulse at 532 nm wavelength was used to illuminate the flow field. The laser sheet was aligned with the mid-span of the test section for measurements in the x–y plane, which coincided with the centre of the nozzle. Scattered light from the tracer particles were captured with a 12-bit FlowSenseEO 4M charge-coupled device camera that has a resolution of 2048 × 2048 pixels and a pixel pitch of 7.4 μm. A camera field of view of 120 × 120 mm was used with an acquisition rate of 4 Hz. The interrogation area size was set to 32 × 32 pixels with 50% overlap in both directions within the x–y plane. The instantaneous images were post-processed using the adaptive correlation option of DynamicStudio developed by Dantec Dynamics. Based on preliminary convergence tests the mean velocities and turbulence statistics were calculated using 4000 instantaneous image pairs. The time between acquisitions of images pairs was set to 0.25 s in order to ensure that consecutive velocity fields were statistically independent.

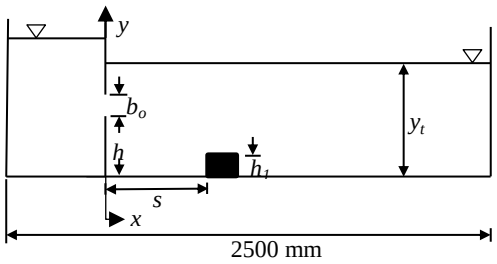

Figure 1. Schematic of experimental setup.

RESULTS

Mean velocity

Contour plots of the streamwise mean velocities (U) are shown in Fig. 2 to reveal the salient features of the mean flow pattern. In this and subsequent contour plots, all flow statistics are normalized by U_o. Results are presented for test cases $R1$ and $R3$ only. In all cases, the vena contracta effect produced by the sharp-edged nozzle caused an acceleration of U. The increase in U occurred in two stages for $R1$. The first stage, caused by the vena-contracta effect, occurred at $x^* \leq 2.6$, and the second stage, caused by the presence of the rib, occurred between $2.8 \leq x^* \leq 4.6$, where $x^* = x/b_o$. The increase in U for $R2$ (not shown) and $R3$ occurred within the regions $x^* \leq 2.2$ and $x^* \leq 3.4$, respectively. The magnitude of maximum reverse velocity within the recirculation region was about $0.02U_o$, $0.21U_o$ and $0.14U_o$ for $R1$, $R2$ and $R3$, respectively. These values are greater than $0.001U_o$ obtained for the reference case where there was no mounted rib. The increased negative velocities can be attributed to an enhanced adverse pressure gradient caused by the presence of the mounted ribs. Also, since the rib was mounted at the reattachment point in the case of $R2$, the leading edge of the rib deflected part of the reattaching fluid into the recirculation region thereby increasing the negative velocity compared to $R1$ and $R3$. A secondary recirculation region was formed beyond the trailing edge of the rib for $R2$ (not shown) and $R3$. This was not the case for $R1$ since it was mounted within the recirculation region of the flow. The length of the recirculation region was estimated as the streamwise location where the mean streamline reattached to the bottom of the channel. The reattachment lengths (L_e) were $4.75b_o$, $7.05b_o$ and $8.60b_o$ for $R1$, $R2$ and $R3$, respectively. The estimated L_e for $R1$ was similar to $L_e = 4.4b_o$ obtained for the reference case. For the $R2$ and $R3$ ribs, secondary reattachment lengths of $3.05b_o$ and $6.0b_o$, respectively, were obtained.

Profiles of U at the following streamwise locations were used to investigate the effects of rib location on the mean flow: s_1, m_1, L_e, and $5h_1$, where the symbols s_1 and m_1 represent the mid-point from the nozzle exit to the leading edge of the rib (0.5s, where s is the distance from the nozzle exit to the leading edge of the rib) and mid-point on top of the rib, respectively. Location $5h_1$ corresponds to 5 rib heights downstream the trailing edge of the rib. The streamwise location s_1 is situated within the recirculation region of the flow. These profiles are shown in Fig. 3(a), and the velocity and length scale used were U_m and b_o, respectively (where U_m is the local streamwise maximum mean velocity). The rib location increased the negative velocities at location s_1. The peak value of U at m_1 for $R3$ occurred at a higher y location compared to both $R1$ and $R2$. This is as a result of deflection of the flow in the wall-normal direction by the rib. Beyond the reattachment point, U profiles for $R2$ and $R3$ developed at a similar rate compared to $R1$. Also, the U profiles for $R2$ and $R3$ at the reattachment point and beyond, showed a considerable spread of the jet compared to $R1$.

The decay of U_m is shown in Fig. 3(b) for the three test cases. There was an initial increase in U_m due to the vena-contracta effect and then a decrease with the minimum value occurring within the vicinity of the rib. The minimum values occurred at about x/b_o = 2.5, 4.5 and 6.0 for $R1$, $R2$ and $R3$, respectively. Beyond these locations, the values of U_m increased to a second peak and then gradually decayed with x/b_o. The second peaks for the jets occurred at $1.8h_1$, $3.0h_1$ and $1.6h_1$ from the trailing edge of the rib for $R1$, $R2$ and $R3$, respectively (where h_1 is the rib height). Increasing the rib location from the nozzle exit resulted in a faster decay of the local maximum streamwise mean velocity. For the streamwise range considered, the decay of U_m after the second peak was similar for $R2$ and $R3$.

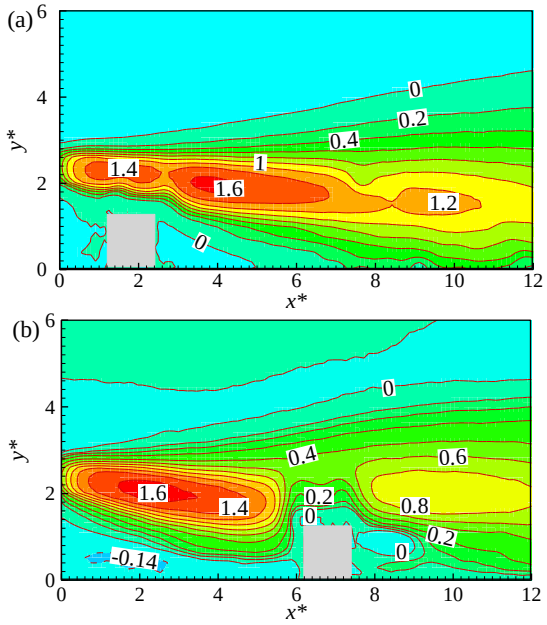

Figure 2. Streamwise mean velocity contours for (a) $R1$ and (b) $R3$ ($x^* = x/b_o$; $y^* = y/b_o$).

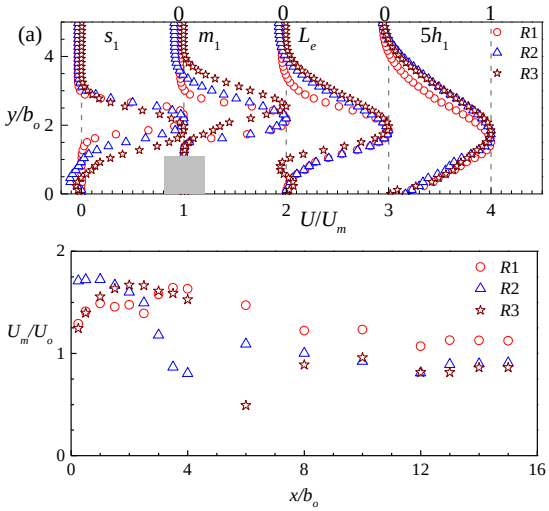

Figure 3. Profiles of (a) U and (b) decay of U_m.

Turbulent kinetic energy and profiles of turbulence statistics

Figure 4 shows contours of the turbulent kinetic energy (k) for $R1$ and $R3$, which was approximated as: $k = 0.75(\overline{u^2}+\overline{v^2})$, since the w component of the fluctuating velocity was not measured. Here u, v and w represent the fluctuating velocity component in streamwise, wall-normal and lateral directions, respectively. The peak value of k occurred at $x^* = 0.5$ for $R1$ and at $x^* = 12$ for both $R2$ and $R3$. The obtained peak values are larger than 0.032 reported by Kasagi and Matsunaga (1995) for a backward-facing step flow. The larger values can be attributed to the formation of a second recirculation region downstream of the ribs as well as enhanced mixing of the jets. In all test cases, k was diffused from the core region of the jet into the outer and inner shear layers. Large scale anisotropy was investigated by evaluating the ratio of $\overline{v^2}$ and $\overline{u^2}$ for the jets. Figure 5 shows that at s_1, high levels of $\overline{v^2}/\overline{u^2}$ occurred at the edges of the jet. As the jet reattached, the ratio of $\overline{v^2}/\overline{u^2}$ decreased. Within the developing region of the flow, the presence of the wall dampened the wall-normal Reynolds normal stress leading to ratios of $\overline{v^2}/\overline{u^2}$ being less than one close to the wall (Durao et al. 1991). Since the distribution of $\overline{v^2}/\overline{u^2}$ is less than one within the flow domain, it suggests that the Reynolds normal stresses are not equal within the early development of the jet. The present results suggest that the flow field of the offset jet is not isotropic.

The effect of rib location on the Reynolds shear stress, $-\overline{uv}$, and wall-normal transport of k and $-\overline{uv}$ are presented in Fig. 6. Within the near field of the jets, the distribution of $-\overline{uv}$ profiles was anti-symmetric which is consistent with the orientation of the mean shear layer. Predominantly positive values of $-\overline{uv}$ were observed at s_1 for all the test cases (Fig. 6a). Changing the rib location from $R1$ to $R2$ and $R3$ resulted in a 34% and 58% decrease in $-\overline{uv}$ values within the recirculation region, respectively. For $R1$, the Reynolds shear stress is significantly larger within the recirculation region compared to the reattached regions. The enhanced levels of the Reynolds shear stress within the recirculation region may be attributed to the predominantly large-scale structures generated due to the separation of the

jet (Etheridge and Kemp, 1978). As a result of mixing and entrainment of the reattached jet, the maximum value of $-\overline{uv}$ decreased with streamwise distance in the case of $R1$. Levels of $-\overline{uv}$ increased for $R2$ and $R3$ at the reattachment point and then subsequently decreased beyond the reattachment point.

The triple velocity correlations are important statistics since their gradients constitute the turbulent diffusion terms in the turbulent kinetic energy and Reynolds stress budget equations. Thus, profiles of the triple velocity correlations can provide guidance to modelling the turbulent diffusion terms in these two transport equations. The triple velocity correlations reported are the transport of k (expressed as $\overline{u^2v} + \overline{v^3}$) and $-\overline{uv}$ (denoted as $-\overline{uv^2}$) in the wall-normal direction as shown in Figs. 6(b) and 6(c) instead of the conventional individual terms. The transport of k was predominantly positive for all test cases at s_1 and m_1 with $R1$ yielding the lowest peak value. The positive values suggest that the diffusion of k was largely from the core region of the jet into the outer shear layer. The transport of $-\overline{uv}$ shown in Fig. 6(c) was also enhanced for $R2$ and $R3$ compared to $R1$. The enhanced transport of $-\overline{uv}$ for both $R2$ and $R3$ can be attributed to the dominance of large-scale structures which may have been as a result of the second recirculation region downstream of the rib.

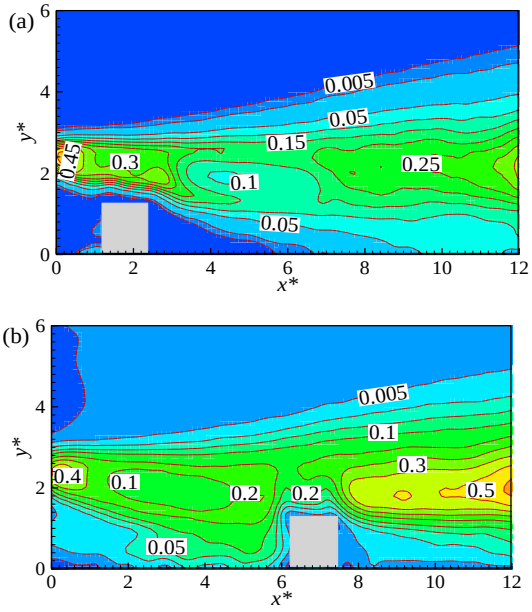

Figure 4. Contours of k for (a) $R1$ and (b) $R3$.

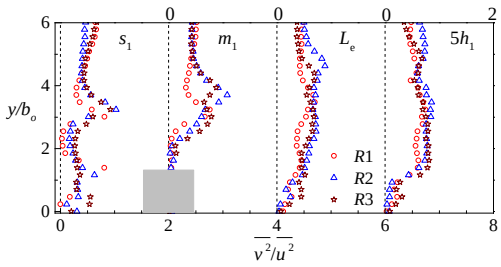

Figure 5. Profiles of stress ratio for the various jets.

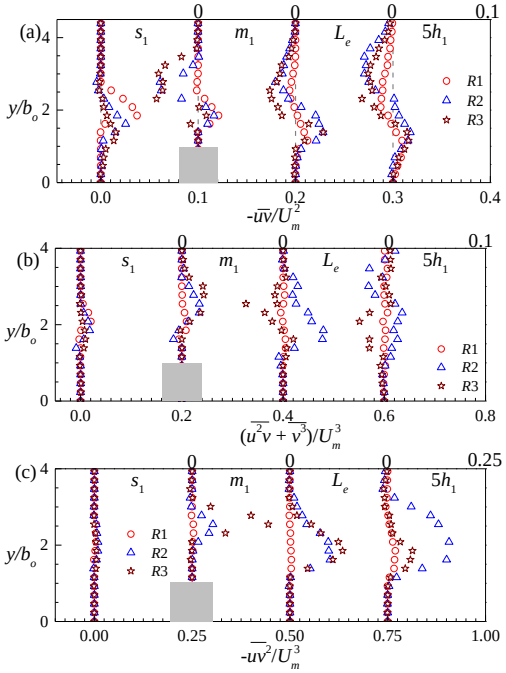

Figure 6. Profile plots of (a) $-\overline{uv}$ (b) wall-normal transport of k and (b) wall-normal transport of $-\overline{uv}$.

Quadrant analysis

The quadrant analysis was used to decompose the active motions that contribute to the Reynolds shear stress. This involves investigating the relationship between the fluctuating velocity components, u and v and sorting them into four different quadrants with $Q1$ ($u > 0$, $v > 0$), $Q2$ ($u < 0$, $v > 0$), $Q3$ ($u < 0$, $v < 0$) and $Q4$ ($u > 0$, $v < 0$) representing the outward interaction, ejection, inward interaction and sweep events, respectively. Following the methodology proposed by Lu and Willmarth (1973), the Reynolds shear stress at each grid point was decomposed into contributions from the four quadrants excluding a hyperbolic hole size, H as follows:

$$\overline{uv}_Q(x,y,H) = \frac{1}{N}\sum_{i=1}^{N} u_i(x,y)v_i(x,y)I_Q(x,y,H)$$

where N is the total number of instantaneous velocity vectors at each grid point and I_Q is the indicator function given by

$$I_Q(x\,y,H) = \begin{cases} 1, \ when\ |u_i(x,y)v_i(x,y)|_Q \geq Hu'(x,y)v'(x,y) \\ 0 \end{cases}$$

For the present analysis, a hole size, $H = 0$ was used. Contours of $Q1$, $Q2$, $Q3$ and $Q4$ are presented for $R1$ and $R3$ in Fig. 7 and Fig. 8, respectively. All four events contributed significantly to the production of Reynolds shear stress according to the orientation of the mean shear layer. In the case of $R1$, the relative peaks of the quadrant events were identical with values of -0.03, 0.05, -0.03 and 0.03 for $Q1$, $Q2$, $Q3$ and $Q4$, respectively. This means that $Q2$ and $Q4$ events contributed 62.5% and 37.5% towards the positive Reynolds shear stress. The result indicates dominance of the ejection events in the Reynolds shear stress production. Changing the location of the rib enhanced contributions from the various events towards the

Reynolds shear stress, with peak values of -0.04, 0.08, -0.08 and 0.04 for $Q1$, $Q2$, $Q3$ and $Q4$, respectively as can be seen from Fig. 8. The present results suggest that both interaction events are relevant to the production of Reynolds shear stress. It is interesting to note from Figs. 7 and 8 that the contribution from both $Q2$ and $Q4$ events to the total Reynolds shear stress close to the nozzle exit was not affected by changing rib location. However, beyond the reattachment point, a more pronounced contribution was observed for the ejection events compared to the sweep events. The ejection events contributed about 50% more towards the Reynolds shear stress compared to the sweep events beyond the reattachment point when the rib location was changed from $R1$ to $R3$. Changing the rib location from $R1$ to $R2$ and $R3$, respectively resulted in a 56% and 50% contribution towards the total $-\overline{uv}$ in $Q2$ quadrant. Profiles of normalized $Q1$, $Q2$, $Q3$ and $Q4$ were extracted at four x locations and presented in Fig. 9. Similar to the contours, all four events contributed immensely towards $-\overline{uv}$. Predominantly larger values of $Q2$ and $Q4$ occurred within the recirculation region for both $R1$ and $R3$. However, contributions from $Q2$ and $Q4$ events decayed further downstream for $R1$. For example, the maxima of $Q2$ decreased by 51% at L_e compared to s_1. In contrast to $R1$, a much larger contribution from all four events occurred at the reattachment point and beyond in the case of $R3$. This can be attributed to the separation of the flow downstream of the rib. At the reattachment point, the peak of $Q2$ and $Q4$ occurred closer to the wall compared to $Q1$ and $Q3$. For example, in the case of $R1$, the peaks of $Q2$ and $Q4$ occurred at y/b_o = 1.42 and 1.15, respectively at the reattachment point. This was lower than y/b_o = 2.62 and 2.26 for $Q1$ and $Q3$, respectively. The present results revealed that the Reynolds shear stress distribution at any streamwise location is influenced by all four quadrant events.

CONCLUSION

A PIV technique was used to investigate the flow characteristics of 3D offset jet flow over surface mounted rib. The experiment was conducted for an offset jet with offset height ratio of 2. The square rib was mounted at three different streamwise locations, $1.25b_o$, $3.45b_o$ and $6.25b_o$ represented herein as $R1$, $R2$ and $R3$, respectively. These locations corresponded to streamwise distances within the recirculation region, mean reattachment point and developing region of the flow, respectively. Contour plots of U revealed that the offset jet accelerated upon discharge as a result of the vena-contracta effect. The distribution of U also revealed enhanced spreading of the jet with increasing rib location. Changing the rib location from $R1$ to $R2$ and $R3$ resulted in a rapid decay of the maximum streamwise mean velocity of the discharged jet. The placement of the rib affected the reattachment length of the discharged jet with reattachment lengths of $4.75b_o$, $7.05b_o$ and $8.60b_o$ recorded for $R1$, $R2$ and $R3$, respectively.

The turbulence statistics (such as k, $-\overline{uv}$ and the triple velocity correlations), were influenced by the rib location. The Reynolds shear stress within the recirculation region of the flow increased by 34% and 58%, respectively, when the rib location was changed from $R1$ to $R2$ and $R3$. Profile plots of the triple velocity correlations indicated that $-\overline{uv}$ was largely transported from the core region of the jet into the outer shear layer. A quadrant analysis was used to decompose the contribution of the active motions towards $-\overline{uv}$. The analysis revealed significant contributions from all four quadrant events. However, the ejection event was the dominant event in all test cases. Changing the rib location from $R1$ to $R2$ and $R3$ resulted in 56% and 50% contribution by the ejection event towards the total $-\overline{uv}$, respectively.

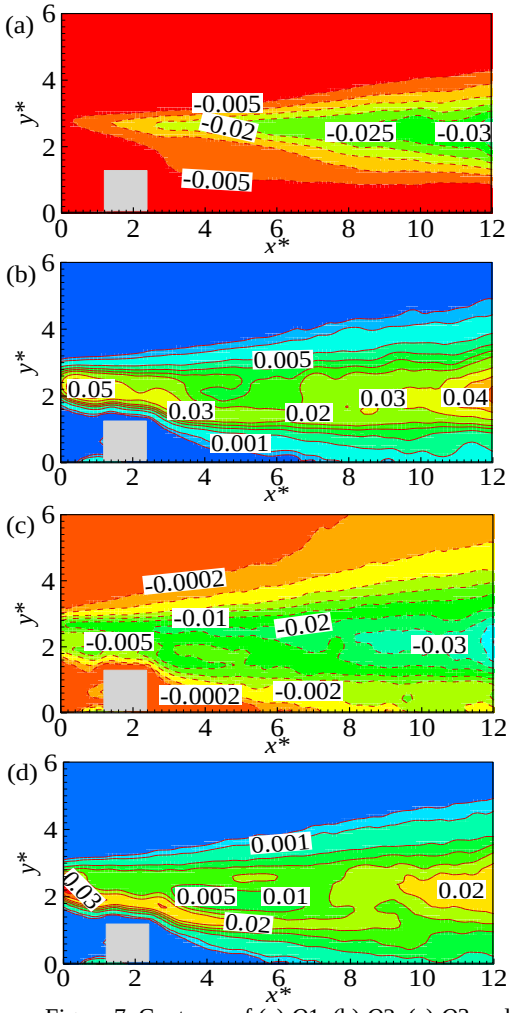

Figure 7. Contours of (a) $Q1$, (b) $Q2$, (c) $Q3$ and (d) $Q4$ for $R1$.

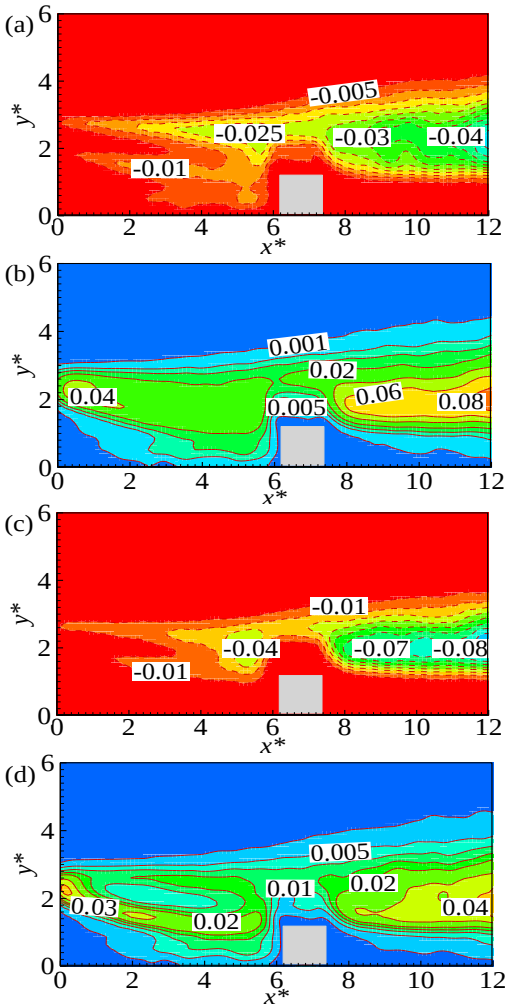

Figure 8. Contours of (a) $Q1$, (b) $Q2$, (c) $Q3$ and (d) $Q4$ for $R3$.

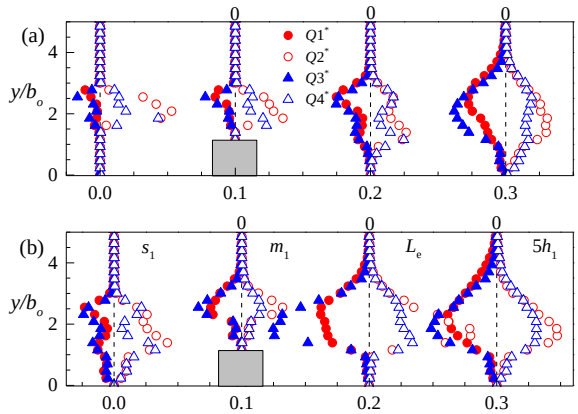

Figure 9. Profiles of all four events for (a) $R1$ and (b) $R3$ at selected streamwise locations.

REFERENCES

Agelinchaab, M., and Tachie, M. F., 2011, "Characteristics of turbulent three-dimensional offset jets", *Journal of Fluids Engineering*, Vol. 133, pp. 051203-1-9.

Antonia, R. A., Browne, L. W., Bisset, D. K., and Fulachier, L., 1987, "A description of the organized motion in the turbulent far wake of a cylinder at low Reynolds number", *Journal of Fluid Mechanics*, Vol. 184, pp. 423-444.

Bhuiyan, F., Habibzadeh, A., Rajaratnam, N., and Zhu, D. Z., 2011, "Reattached turbulent submerged offset jets on rough beds with shallow tailwater", *Journal of Hydraulic Engineering*, Vol. 137, pp. 1636-1648.

Durao, D., Gouveia, P., and Pereira, J., 1991, "Velocity characteristics of the flow around a square cross section cylinder near a channel wall", *Experiments in Fluids*, Vol. 350, pp. 341-350.

Etheridge, D. W., and Kemp, P. H., 1978, "Measurements of turbulent flow downstream of a rearward-facing step", *Journal of Fluid Mechanics*, Vol. 86(3), pp. 545-566.

Kasagi, N., and Matsunaga, A., 1995, "Three-dimensional particle-tracking velocity measurement of turbulence statistics and energy budget in a backward-facing step flow", *International Journal of Heat and Fluid Flow*, Vol. 16, pp. 477-485.

Lu, S. S., and Willmarth, W. W., 1973, "Measurement of the structure of the Reynolds stress in a turbulent boundary layer", *Journal of Fluid Mechanics*, Vol. 60(3), pp. 481-511.

Nasr, A., and Lai, J. C. S., 1998, "A turbulent plane offset jet with small offset ratio", *Experiments in Fluids*, Vol. 24, pp. 47-57.

Nyantekyi-Kwakye, B., Clark, S., Tachie, M. F., Malenchak, J., and Muluye, G., 2014, "Flow characteristics within the recirculation region of 3D turbulent offset jet", *Journal of Hydraulic Research*, pp. 1-13.

Pelfrey, J. R. R., and Liburdy, J. A., 1986, "Mean flow characteristics of a turbulent offset jet", *Transactions of the ASME*, Vol. 108, pp. 82-88.